PHYSICAL REVIEW B **106**, 125135 (2022)

Quasinodal spheres and the spin Hall effect: The case of YH_3 and CaTe

Rafael González-Hernández,[1,2,*] Carlos Pinilla,[1,3,†] and Bernardo Uribe[4,5,‡]
[1] *Departamento de Física y Geociencias, Universidad del Norte, Km. 5 Vía Antigua Puerto Colombia, Barranquilla 080020, Colombia*
[2] *Institut für Physik, Johannes Gutenberg Universität Mainz, D-55099 Mainz, Germany*
[3] *School of Chemistry, University of Bristol, Cantock's Close, Bristol BS8 1TS, United Kingdom*
[4] *Departamento de Matemáticas y Estadística, Universidad del Norte, Km. 5 Vía Antigua Puerto Colombia, Barranquilla 080020, Colombia*
[5] *Max Planck Institut fuer Mathematik, Vivatsgasse 7, 53115 Bonn, Germany*

(Received 30 April 2022; revised 12 July 2022; accepted 9 September 2022; published 21 September 2022)

Band inversion is a known feature in a wide range of topological insulators characterized by a change of orbital type around a high-symmetry point close to the Fermi level. In some cases of band inversion in topological insulators, the existence of quasinodal spheres has been detected, and the change of orbital type is shown to be concentrated along these spheres in momentum space. To understand this phenomenon, we develop a local effective fourfold Hamiltonian that models the band inversion and reproduces the quasinodal sphere. This model shows that the signal of the spin Hall conductivity, as well as the change of orbital type, are both localized on the quasinodal sphere, and moreover, that these two indicators characterize the topological nature of the material. Using K-theoretical methods, we show that the change of orbital type parametrized by an odd clutching function is equivalent to the strong Fu-Kane-Mele invariant. We corroborate these results with *ab initio* calculations for the materials YH_3 and CaTe, where in both cases the signal of the spin Hall conductivity is localized on the quasinodal spheres in momentum space. We conclude that a nontrivial spin Hall conductivity localized on the points of change of orbital type is a good indicator for topological insulation.

DOI: 10.1103/PhysRevB.106.125135

I. INTRODUCTION

The incursion of topological invariants in condensed-matter physics has led to an enhanced classification of quantum materials [1–4]. Among the insulators, the topological insulators (TIs) have attracted significant attention due to the presence of conducting surface states and because they show efficient spin transport properties [5–8]. The presence of these unique surface states, together with the topological Fu-Kane-Mele invariant, have been used to characterize these topological insulator phases from normal insulator systems [9–11].

The topological order of some insulators may be alternatively deduced from the change of orbital type on the last valence bands around a time-reversal invariant point (TRIM). This feature is known in the literature as "band inversion," and it has been used extensively to classify TIs [4,12,13]. Band inversion is assumed to be induced from band splitting due to strong spin-orbit coupling (SOC) interaction from heavy elements in materials [14–18]. In these systems, SOC can have a significant impact on the band structure, and it induces an opening gap between the conduction and valence bands, thus changing the orbital type. This band inversion may be coupled with a change in the inversion symmetry eigenvalues at the appropriate TRIM. It was this precise feature that led to the establishment of the Fu-Kane-Mele invariant in topological insulators with inversion symmetry as Bi_2Se_3, Bi_2Te_3, and Sb_2Te_3 [19,20]. However, some materials show that the band inversion can appear spontaneously, or it may be induced by strain, even without SOC interaction [12,21]. This phenomenon can be observed in α-Sn, HgTe, and several half-Heusler and chalcopyrite semiconductors, where the band inversion is presented at a particular TRIM and independent of the SOC interaction [22–26].

The type of band inversion that is of interest for this work appears whenever there is a hybridization of the energy bands, and the change of orbital type is concentrated on the **k**-states where the energy gap is opened. This form of band inversion is present, among others, on the trihydrides materials, and it has been previously reported in Refs. [27,28]. On these materials, a small energy gap is present, and the **k**-states with a small energy gap form a two-dimensional sphere. In [28] these spheres were called "pseudo Dirac nodal spheres" (PDNSs), and here we have denoted them as "quasinodal spheres." In the pioneering work by Wang *et al.* [28], the possible formation of PDNSs in crystal structures is reported on different symmetry point groups through the study of band crossings with pairs of one-dimensional (1D) irreducible representations. It is also found that the PDNS phase is robust against the SOC effect, in particular for the MH_3 (with $M = $ Y, Ho, Tb, Nd) and Si_3N_2 materials. In addition, the prediction of a realizable topological state with exotic transport properties is suggested for these PDNS prototypes [28]. The analysis of the topological nature and the spin transport properties of the PDNS (or quasinodal spheres) has remained an open question, and it has been one of the motivations of the present work.

In this work, we study the mechanism underlying the band inversion occurring through hybridization as it happens on

---

[*] rhernandezj@uninorte.edu.co

[†] ccpinilla@uninorte.edu.co

[‡] bjongbloed@uninorte.edu.co; uribe@mpim-bonn.mpg.de

trihydrides. We argue that the change of orbital type is concentrated on the quasinodal sphere, and moreover, that the Fu-Kane-Mele invariant characterizing the TI property of the material can be deduced from the nontriviality of the spin Hall conductivity (SHC) and the localization of its signal on the quasinodal sphere. This fact explains the two-dimensional nature of the **k**-points where hybridization is happening, and it shows how the Fu-Kane-Mele invariant relates to the SHC and the change of orbital type.

The paper contains two main parts, namely the theoretical analysis and the material realization. In the first part, we analyze the mechanism of band inversion by using a fourfold effective Hamiltonian for a system in which the orbital character change is present, the quasinodal sphere is induced, and both the signal of the SHC and the orbital type change are concentrated on the quasinodal sphere. Here we show explicitly how the valence states of the effective Hamiltonian define an element in the appropriate K-theory, and how this K-theoretical element matches the K-theoretical version of the strong Fu-Kane-Mele invariant. In the second part, we investigate two possible materials, yttrium trihydride (YH_3) and calcium telluride (CaTe), which show an efficient spin/change conversion generated from the band inversion on the quasinodal sphere.

II. BAND INVERSION

Let us consider a Hamiltonian with time-reversal symmetry $\mathbb{T}$ and inversion symmetry $\mathcal{I}$ where spin-orbit coupling is taken into account. Band inversion could be understood as the change of orbital character on the last valence bands around a time-reversal-invariant point (TRIM). This change of character, whenever coupled with a change of eigenvalue of the inversion operator, determines the strong topological insulator nature of the material.

In the case of interest, the change of orbital type is occurring on a sphere of points where the energy gap is small. This two-dimensional sphere in momentum space with a small energy gap (comparable to room temperature ~ 25 meV) has been coined a *quasinodal sphere*, generalizing the concept of a quasinodal line that was presented by the first and third authors in [29].

In what follows, we argue that band inversion due to hybridization produces a quasinodal sphere on momentum space where orbital characters are mixed, and moreover, where the Fu-Kane-Mele invariant can be extracted. We first define a local model for the low-energy effective Hamiltonian inducing band inversion due to hybridization, next we calculate its quasinodal sphere together with a 2×2 matrix information on each point obtained from the change of orbital type on the valence bands, and finally we relate these parametrized matrices to the topological invariants obtained through K-theory.

A. Model Hamiltonian

Take the Pauli matrices τ_i and σ_j in orbital and spin coordinates, respectively, and consider the Hamiltonian

$$H(\mathbf{k}) = M(\mathbf{k})\tau_3\sigma_0 + A(\mathbf{k})\tau_1\sigma_3 + B(\mathbf{k})\tau_2\sigma_0, \qquad (1)$$

where

$$M(\mathbf{k}) = D_1 - m_1k_z^2 - n_1\left(k_x^2 + k_y^2\right), \qquad (2)$$

$$A(\mathbf{k}) = D_2k_z + E_2k_z^3 + F_2\left(3k_x^2k_y - k_y^3\right), \qquad (3)$$

$$B(\mathbf{k}) = D_3\left(k_x^3 - k_xk_y^2\right). \qquad (4)$$

This Hamiltonian preserves time reversal, inversion, and a threefold rotation with matrices

$$\mathbb{T} = i\tau_0\sigma_2\mathbb{K}, \quad \mathcal{I} = -\tau_3\sigma_0, \quad \text{and } C_3 = e^{i\tau_0\sigma_3\frac{\pi}{3}}, \qquad (5)$$

respectively. Here, C_3 is a threefold rotation around the z-axis. The bands are doubly degenerate due to the presence of both time reversal and inversion, and the energies of the bands are

$$\pm E(\mathbf{k}) = \pm\sqrt{M(\mathbf{k})^2 + A(\mathbf{k})^2 + B(\mathbf{k})^2}. \qquad (6)$$

Tuning up the constants to locally model the band inversion present in YH_3 at the point Γ, we set the coefficients to the following values:

$$\begin{aligned} D_1 &= 0.2, \quad m_1 = n_1 = 18, \\ D_2 &= 0.1, \quad E_2 = F_2 = D_3 = 5. \end{aligned} \qquad (7)$$

The energy bands of the Hamiltonian are presented in Figs. 1(a) and 1(b) together with their projections on the first orbital. There is no symmetry protecting energy crossings and therefore the eigenstates hybridize producing an energy gap. The change of orbital type is concentrated along the points in momentum space whose energy gap is small, and they define a two-dimensional sphere, as can be seen in Fig. 1(d). This two-dimensional sphere is a quasinodal sphere, and it is necessary for the band inversion that induces the Hamiltonian. Note that the inversion operator $\mathcal{I} = -\tau_3\sigma_0$ is coupled with the orbital types since it acts by -1 on the first orbital and by $+1$ on the second orbital [see Fig. 1(a)]. The interdependence of the inversion operator with the orbit type is what permits us to distinguish the TI nature of the material by the change of eigenvalues of the inversion. Nevertheless, the TI nature of the material is kept while inversion is broken, thus the change of orbital type, together with the SHC, is what allows us to distinguish its topological nature. From Fig. 1(d), we see that the valence bands are concentrated on the second orbital inside the quasinodal sphere while concentrated on the first orbital outside of it.

The change of orbital type of the valence bands along the quasinodal sphere permits us to define a 2×2 unitary complex matrix for each point on the nodal sphere. This assignment produces a map from the sphere S^2 to the Lie group of special unitary matrices SU(2), which is equivariant with respect to the inversion operator. Here the inversion operator acts by the antipodal action on the sphere and by multiplication by -1 on SU(2). This map can be understood as the clutching map [in the words of Atiyah (Ref. [30], p. 20)] that defines the rank 2 complex vector bundle over the three-dimensional sphere, which produces the nontrivial Fu-Kane-Mele invariant. Let us postpone the construction of the Fu-Kane-Mele invariant on the three-dimensional sphere to the next section, and let us show how the matrices are defined.

Denote by $\varphi^i_\pm(\mathbf{k})$, $i \in \{1, 2\}$, the four eigenvectors of the Hamiltonian of Eq. (1) with the fixed parameters described in

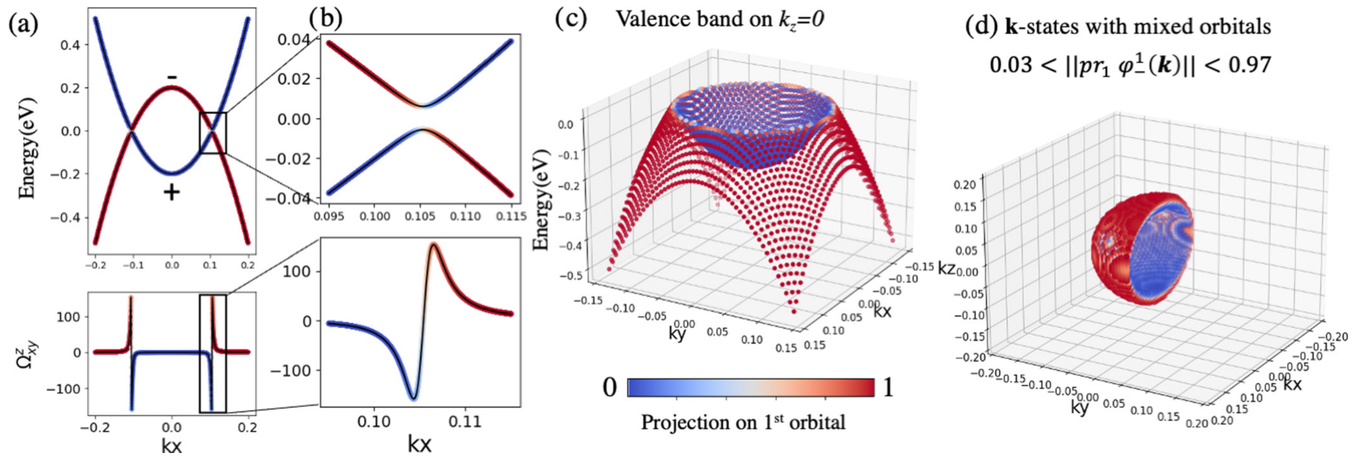

FIG. 1. Energy bands of the Hamiltonian of Eq. (1) with projection to the first orbital. (a) Top panel: valence and conduction bands on k_x coordinate axis with projection on the first orbital. The eigenvalues of the inversion operator at (0,0,0) on the valence bands are +1 and on the conduction bands are −1. Bottom panel: sum of the spin Berry curvatures of the two valence bands Ω^z_{xy}. (b) Top panel: closeup view of the energy bands where the change of orbital type is concentrated. Bottom panel: closeup view of the sum of the spin Berry curvatures Ω^z_{xy}. The signal of the spin Berry curvature is concentrated where the change of orbital type occurs. (c) Valence band on the plane $k_z = 0$ with projection on the first orbital. (d) **k**-states with mixed orbital type (more than 3% of each orbital type, $k_y \leqslant 0$) equivalent to the quasinodal sphere with an energy gap of less than 0.05 eV. The color represents the magnitude of the projection on the first orbital. Inside the quasinodal sphere, the states are concentrated on the first orbital, while outside they are concentrated on the second orbital.

Eqs. (7) satisfying the equation

$$H(\mathbf{k})\varphi^i_\pm(\mathbf{k}) = \pm E(\mathbf{k})\varphi^i_\pm(\mathbf{k}). \tag{8}$$

Note that the valence states $\varphi^i_-(\mathbf{k})$ are well defined for all **k** since the system is gapped, and therefore we may take the vector projections of each valence state to the first and second orbital, respectively. The eigenstates have four coordinates,

$$\varphi^i_- = (\varphi^i_{-,1}, \varphi^i_{-,2}, \varphi^i_{-,3}, \varphi^i_{-,4}) \in \mathbb{C}^4, \tag{9}$$

and the projection on the first orbital takes the first two coordinates and the projection on the second takes the last two. Denoting as pr_j the projection on the jth orbital, we have

$$\mathrm{pr}_1\varphi^i_- = (\varphi^i_{-,1}, \varphi^i_{-,2}), \tag{10}$$

$$\mathrm{pr}_2\varphi^i_- = (\varphi^i_{-,3}, \varphi^i_{-,4}). \tag{11}$$

Along the quasinodal sphere both projections are nontrivial [we may take the sphere of radius $||\mathbf{k}|| = 0.11$; see Fig. 1(c)], and therefore we may define the following matrix coefficients:

$$A_{ij}(\mathbf{k}) = (-1)^i \left\langle \frac{\mathrm{pr}_1\varphi^i_-(\mathbf{k})}{||\mathrm{pr}_1\varphi^i_-(\mathbf{k})||} \middle| \frac{\mathrm{pr}_2\varphi^j_-(\mathbf{k})}{||\mathrm{pr}_2\varphi^j_-(\mathbf{k})||} \right\rangle \tag{12}$$

for $i, j \in \{1, 2\}$. Since the composition $\mathbb{T}\mathcal{I}$ commutes with the Hamiltonian, we may consider φ^2_- to be the Kramers pair of φ^1_- satisfying the equation

$$\varphi^2_- = \mathbb{T}\mathcal{I}\varphi^1_-. \tag{13}$$

From Eqs. (5) we know that $\mathbb{T}\mathcal{I} = -i\tau_3\sigma_2\mathbb{K}$, and therefore Eq. (13) implies the following equality:

$$(\varphi^2_{-,1}, \varphi^2_{-,2}, \varphi^2_{-,3}, \varphi^2_{-,4}) = (-\overline{\varphi}^1_{-,2}, \overline{\varphi}^1_{-,1}, -\overline{\varphi}^1_{-,4}, \overline{\varphi}^1_{-,3}). \tag{14}$$

Replacing Eq. (14) on the definition of the matrix coefficients of Eq. (12) we see that the matrix A is unitary with $A_{11} = \overline{A}_{22}$, $A_{12} = -\overline{A}_{21}$, and its determinant is 1. Hence the matrix A belongs to the Lie group SU(2) of special unitary matrices.

If we take $S^2_r = \{\mathbf{k} : ||\mathbf{k}|| = r\}$ to be the quasinodal sphere of the system [$r = 0.11$ for the Hamiltonian with parameters in Eqs. (7)], we obtain a map

$$A : S^2_r \to \mathrm{SU}(2), \quad \mathbf{k} \mapsto A(\mathbf{k}). \tag{15}$$

The explicit form of the inversion operator $\mathcal{I} = -\tau_3\sigma_0$ implies the following equation:

$$\mathrm{pr}_j\varphi^i_-(\mathbf{k}) = (-1)^j \mathrm{pr}_j\varphi^i_-(-\mathbf{k}), \ \ j \in \{1, 2\}, \tag{16}$$

which makes the map A equivariant with respect to the inversion action, i.e.,

$$A(-\mathbf{k}) = -A(\mathbf{k}). \tag{17}$$

Any equivariant map such as A produces the Fu-Kane-Mele invariant since any two maps satisfying Eq. (17) are homotopic (Ref. [31], Lemma 3.27). In particular, the map A is homotopic to the map $C : S^2_r \to \mathrm{SU}(2)$,

$$C(\mathbf{k}) = \begin{pmatrix} ik_z & k_x + ik_y \\ -k_x + ik_y & -ik_z, \end{pmatrix}, \tag{18}$$

which is a simple clutching function that defines the rank 2 bundle with a nontrivial Fu-Kane-Mele invariant.

Another important feature of the quasinodal sphere of this Hamiltonian is the fact that the signal for the spin Hall conductivity Ω^z_{xy} localizes around it. In Fig. 1(d), we have plotted the points on which the orbital type is mixed, i.e., **k**-points with more than 3% on each orbital,

$$0.03 < ||\mathrm{pr}_1\varphi^1_-(\mathbf{k})|| < 0.97, \tag{19}$$

and we notice that these mixed states define the quasinodal sphere. From Fig. 1(b) we notice that the signal of the SHC

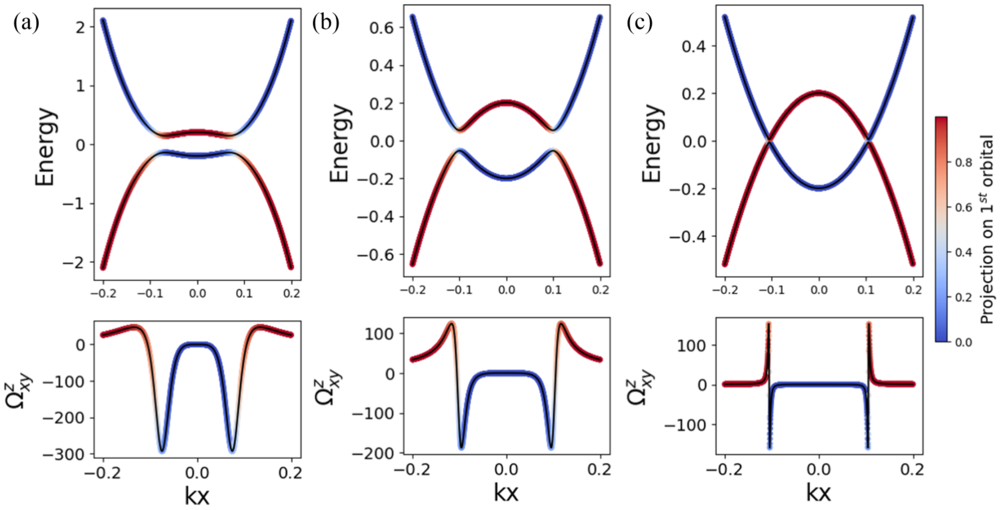

FIG. 2. Spin Berry curvature Ω^z_{xy} at the Fermi level with respect to k_x of the Hamiltonian of Eq. (1). The energy gap is widened by setting the structural constants E_2, F_2, D_3 of the Hamiltonian to the following values: (a) $E_2 = F_2 = D_3 = 250$, (b) $E_2 = F_2 = D_3 = 50$, and (c) $E_2 = F_2 = D_3 = 5$. The values of (c) are the original values from Eq. (7). The signal of the SHC is concentrated on the region where the orbital type changes. Note that despite the fact that the difference of energies appears on the denominator of the Kubo formula of the SHC [see Eq. (36)], the signal of the spin Berry curvature localizes whenever the change of orbit type occurs.

is localized on the **k**-points with mixed orbital type. This feature could be appreciated on the materials YH_3 and CaTe in Figs. 3(d), 3(f) and 3(g), and Figs. 4(d), 4(f) and 4(g), respectively.

The topological invariant that the Hamiltonian of Eq. (1) defines can be better understood with the help of *K*-theory. This is the subject of the next section.

B. *K*-theory, clutching functions, and sewing matrices

Restrict the Hamiltonian to a ball *B* centered at the origin, which includes the quasinodal sphere. The valence eigenstates define a rank 2 complex vector bundle over *B* that incorporates the clutching function *A*. This bundle possesses the topological information to capture the Fu-Kane-Mele invariant, but unfortunately it does not trivialize on the boundary of *B* in order to define an appropriate element in *K*-theory [the

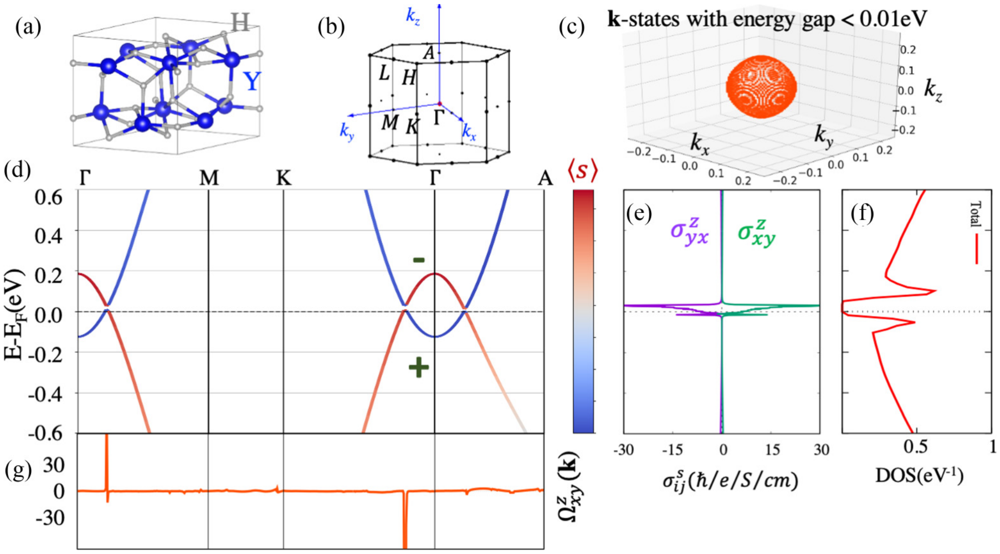

FIG. 3. (a) Ball stick model of the hexagonal crystal structure of YH_3 material [39]. (b) Hexagonal Brillouin zone indicating the high-symmetry points. (c) Position of electronic states in reciprocal space with an energy band gap of less than 0.01 eV. (d) Projected band structure with H-*s* orbitals along the high-symmetry lines, where the symbols + and − indicate the inversion symmetry eigenvalues of +1 and −1, respectively, at the Γ point. (e) Spin Hall conductivity (in ħ/*e*/S/cm). (f) Total density of states (DOS) as a function of Fermi energy. (g) Spin Berry curvature $\Omega^z_{xy}(\mathbf{k})$ [Å^2] along high-symmetry lines added over the valence band. The $\Omega^z_{xy}(\mathbf{k})$ signal is concentrated where the change of orbital character occurs. It is noted there is a large SHC in the band gap where there are no electronic states. Spin-orbit coupling is included in all the calculations and the Fermi level is set to zero.

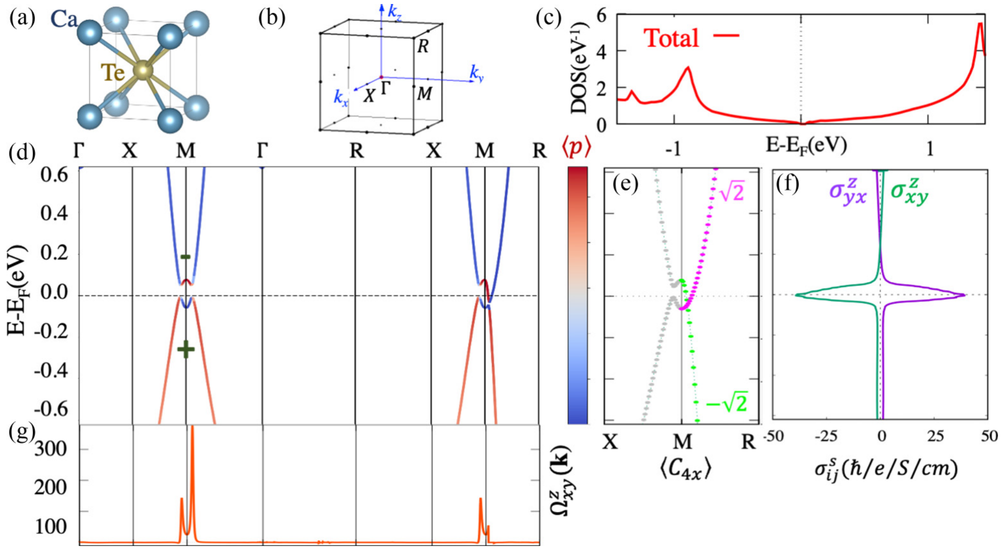

FIG. 4. (a) Crystal structure [39] and (b) cubic Brillouin zone indicating the high-symmetry points of the CaTe material (cubic phase). (c) Total density of states (DOS) as a function of Fermi energy. (d) Projected band structure with Ca-p orbitals along the high-symmetry lines, where the symbols + and − denote the inversion symmetry eigenvalues at the M point, +1 and −1, respectively. (e) C_{4z} symmetry eigenvalues resolved at the electronic bands along the X-M-R k-path. (f) Spin Hall conductivity (in $\hbar/e/$S/cm) as a function of Fermi energy. It is noted there is a strong SHC signal at the Fermi level, which is attributed to the quasinodal sphere and the Dirac point. (g) Spin Berry curvature $\Omega^z_{xy}(k)$ (Å^2) along high-symmetry lines added over the valence band. The $\Omega^z_{xy}(k)$ signal is concentrated where the change of orbital character occurs. Spin-orbit coupling is included in all the calculations, and the Fermi level is set as zero.

Hamiltonian of Eq. (1) provided only a local model, and it was not defined over a compact space]. To overcome this issue, we will construct a rank 2 complex vector bundle over the sphere S^3 which models the structure of the valence eigenstates of the Hamiltonian of Eq. (1), and we will show that this vector bundle incorporates the Fu-Kane-Mele invariant for K-theory. This bundle will model the K-theoretical properties of the valence states, and it will permit us to calculate its topological invariants.

Consider the three-dimensional sphere

$$S^3 = \{(t, k_1, k_2, k_3) | t^2 + ||k||^2 = 1\}, \tag{20}$$

where $S^3\backslash\{(-1, \mathbf{0})\}$ could be thought of as the stereographic projection of the ball B, and S^3 is its one-point compactification. Take $\rho : [-1, 1] \to [0, 1]$ a partition of unity on the interval $[-1, 1]$ with $\rho|_{[-1,-1+\varepsilon)} = 0$ and $\rho|_{(1-\varepsilon,1]} = 1$ for small ε. Define the rank 2 vector bundle $E \subset S^3 \times (\mathbb{C}^2)^2$ by the equation

$$E = \{[(t, \mathbf{k}), (\rho(t)u, (1 - \rho(t))C(\mathbf{k})u)] \mid u \in \mathbb{C}^2\}, \tag{21}$$

and define the actions of $\mathcal{I}$ and $\mathbb{T}$ as in Eqs. (5) by the following formulas:

$$\mathcal{I} \cdot ((t, \mathbf{k}), (u, v)) = ((t, -\mathbf{k}), (-u, v)), \tag{22}$$

$$\mathbb{T} \cdot ((t, \mathbf{k}), (u, v)) = ((t, -\mathbf{k}), (\mathbb{J}u, \mathbb{J}v)). \tag{23}$$

Here $\mathbb{J} = i\tau_2\mathbb{K}$ commutes with the matrices in SU(2) and therefore the action of $\mathbb{T}$ is well-defined. Moreover, the partition of unity ρ could be understood as the projection map on the first orbital while $(1 - \rho)$ could be understood as the projection on the second.

When the action of $\mathcal{I}$ is disregarded, the relative bundle $[E] - [S^3 \times \mathbb{C}^2]$ generates the only nontrivial class on the appropriate relative K-theory groups. Choosing as base point $(-1, \mathbf{0})$ and following the notation of Ref. [31] (Appendix C), we have that

$$[E] - [S^3 \times \mathbb{C}^2] \in \widetilde{KQ}^0(S^3) \cong \mathbb{Z}/2, \tag{24}$$

and therefore the bundle E induces the strong Fu-Kane-Mele invariant. Here $KQ^{n+4} \cong KR^n$, where KR^* is Atiyah's real K-theory [32], and

$$\widetilde{KQ}^0(S^3) \cong \widetilde{KR}^4(S^3) \cong KR^7(*) \cong KO^{-1} \cong \mathbb{Z}/2. \tag{25}$$

Taking into account the involution $\mathcal{I}$, the relative bundle $[E] - [S^3 \times \mathbb{C}^2]$ gives the generator of the relative equivariant symplectic K-theory groups:

$$[E] - [S^3 \times \mathbb{C}^2] \in \widetilde{KSp}^0_{\langle\mathcal{I}\rangle}(S^3) \cong \mathbb{Z}. \tag{26}$$

Here the composition $\mathcal{I}\mathbb{T}$ defines the quaternionic structure on the fibers of the bundle, and $\mathcal{I}$ induces a $\mathbb{Z}/2$-equivariant quaternionic action on the bundle. The groups $\widetilde{KSp}^0_{\langle\mathcal{I}\rangle}(S^3)$ are the reduced $\mathbb{Z}/2$-equivariant symplectic K-theory groups of the sphere S^3 [33]; cf. [34]. The restriction map to the point $(1, \mathbf{0})$ counts the number of quaternionic $\mathbb{Z}/2$-representations with ±1-eigenvalues:

$$\widetilde{KSp}^0_{\langle\mathcal{I}\rangle}(S^3) \to \mathbb{Z}_{-1} \oplus \mathbb{Z}_{+1} \cong KSp^0_{\langle\mathcal{I}\rangle}(\{(1, \mathbf{0})\}), \tag{27}$$

$$E \mapsto 1 \oplus 0, \tag{28}$$

where $\mathbb{Z}_{-1}$ counts the nontrivial ones and $\mathbb{Z}_{+1}$ counts the trivial ones. Since this restriction map is injective, the topological class of the bundle can be determined by the eigenvalues of $\mathcal{I}$ on the fixed point set of the action. Since E has the nontrivial quaternionic $\mathbb{Z}/2$-representation on the fixed point $(1, \mathbf{0})$ and the trivial one on $(-1, \mathbf{0})$, the strong Fu-Kane-Mele invariant can be determined by the parity of the number of pairs of complex -1 eigenvalues on the fixed points of the $\mathcal{I}$ action; this is the main result of Fu *et al.* [9].

The restriction of the bundle E to the sphere of points with $t = 0$ permits us to define the transformation from the first to the second orbital, and this transformation is precisely the function C presented in Eq. (18). This clutching function is shown in Ref. [31] (Corollary 4.1) to induce the Fu-Kane-Mele invariant.

The bundle E models the topological structure of the valence states of the Hamiltonian of Eq. (1), and it induces the topological generators in both the equivariant symplectic K-theory and the quaternionic K-theory of involution spaces. Hence the bundle E models the topological nature of the band inversion, and it induces the strong Fu-Kane-Mele invariant [9]. The change of eigenvalues of the inversion operator on the fixed points on the sphere S^3 is only possible whenever the clutching function C is defined on the sphere S^2 and it is odd [Eq. (17)].

The relation of the clutching functions with the SHC can be seen in Fig. 2. The signal of the SHC concentrates on the points where the change of orbital type occurs despite the size of the energy gap. We can therefore conclude that not only do the $\mathbf{k}$-points with mixed orbital type make the quasinodal sphere, but moreover the signal of the spin Hall conductivity localizes on this quasinodal sphere.

We can go one step further and we may calculate the sewing matrices of the inversion and the time-reversal operator. For this we need to take a trivialization of the bundle E (since any rank 2 complex bundle over S^3 is trivializable), and we may write the inversion and the time-reversal operator on the new basis. Now we have $E = S^3 \times \mathbb{C}^2$, and the actions become

$$\mathcal{I} \cdot ((t, \mathbf{k}), u) = ((t, -\mathbf{k}), (t\mathrm{Id} + C(\mathbf{k}))u), \tag{29}$$

$$\mathbb{T} \cdot ((t, \mathbf{k}), u) = ((t, -\mathbf{k}), (t\mathrm{Id} + C(\mathbf{k}))\mathbb{J}u). \tag{30}$$

For (e_1, e_2) the canonical basis on $\mathbb{C}^2$, the sewing matrices for the operator P on E are defined by the equation

$$G(P)_{ij}(t, \mathbf{k}) = \langle e_i | P(t, \mathbf{k}) | e_j \rangle. \tag{31}$$

For the inversion and the time-reversal operator, the sewing matrices can be described as follows:

$$G(I)(t, \mathbf{k}) = t\mathrm{Id} + C(\mathbf{k}), \tag{32}$$

$$G(\mathbb{T})(t, \mathbf{k}) = [t\mathrm{Id} + C(\mathbf{k})]\mathbb{J}. \tag{33}$$

In both cases, the sewing matrices define maps from S^3 to SU(2) whose degree is ± 1. From [35–37] we know that the parity of the degree of those maps recovers the Chern-Simons axion coupling term

$$\theta = \frac{1}{4\pi} \int_{\mathrm{BZ}} dk^3 \epsilon^{\alpha\beta\gamma} \mathrm{Tr}\left(\mathcal{A}_\alpha \partial_\beta \mathcal{A}_\gamma - \frac{2i}{3} \mathcal{A}_\alpha \mathcal{A}_\beta \mathcal{A}_\gamma \right). \tag{34}$$

Since the parity of the degrees of both $G(I)$ and $G(\mathbb{T})$ is odd, we know that $\theta = \pi$. Hence we see the topological nature of the trivial complex bundle E whenever the action of either I or $\mathbb{T}$ is defined as in Eqs. (29) and (30).

Note that whenever $t = 0$, both the clutching function of the bundle of Eq. (21) and the sewing matrices of the inversion operator agree. The topological nature of the bundle could be theoretically deduced then from either one. Unfortunately, both approaches are not well suited for computational calculations. On the one hand, the definition of the clutching functions is not gauge-invariant, and on the other, the calculation of the Chern-Simons coupling term has been elusive up to now for real materials [38]. We hope in the future that new methods are developed to calculate both.

III. MATERIAL REALIZATION

A. Yttrium trihydride

The yttrium trihydride ($\mathrm{YH_3}$) compound can crystallize in a hexagonal structure with space group P-3c1 no. 165 [40], as shown in Fig. 3(a). This space group contains 12 symmetry operations that can be generated by the rotation C_{3z}, the screw rotation $S_{2(x+y)}$, the inversion $\mathcal{I}$, and the time-reversal $\mathbb{T}$ symmetry operations. The presence of both $\mathcal{I}$ and $\mathbb{T}$ symmetries indicates that energy bands are doubly degenerate along the full Brillouin zone (BZ). The BZ for this material is a hexagonal unit cell in reciprocal space with high-symmetry points as indicated in Fig. 3(b).

Based on *ab initio* calculations, we have obtained the electronic band structure of the $\mathrm{YH_3}$ material, and we have confirmed the appearance of the quasinodal sphere centered at the Γ point. The band structure along the high-symmetry lines, including the spin-orbit coupling interaction, is shown in Fig. 3(d). It should be noted there is a hybridization band gap between the valence and conduction bands for all $\mathbf{k}$-paths that connect the Γ point with any other high-symmetry point. The hybridization band gap is originated by the SOC interaction, and it is extended along the quasinodal sphere in reciprocal space. Symmetry analysis indicates that no crystal symmetry protects a possible nodal sphere or line whenever SOC is included. To confirm the existence of the quasinodal sphere, we carried out a systematic search of the $\mathbf{k}$-points in the BZ where almost zero band gaps between the occupied and unoccupied bands are located. To visualize the quasinodal sphere, we have plotted the $\mathbf{k}$-points in the BZ with an energy band gap of less than 0.01 eV in Fig. 3(c).

The orbital-resolved H-s projection is also shown in the band structure of Fig. 3(d). The figure shows that these orbitals dominate the valance band close to the Fermi level. In addition, a band inversion (change of the orbital character) is noted around the Γ point, which is occurring on the surface of the quasinodal sphere, as was predicted by the $\mathbf{k} \cdot \mathbf{p}$ model presented in the previous section.

We have also calculated the inversion symmetry eigenvalues on all TRIMs, and we have observed the change of eigenvalues from the valence to the conduction bands at the Γ point [symbols + and − in Fig. 3(d)]. This change of eigenvalues indicates that the material can be considered a topological insulator with a tiny band gap spread along the quasinodal sphere. We have corroborated the topological insulator property of this material by using the Wilson loop method in order to find the $\mathbb{Z}_2$ invariants for the six k_i planes in the BZ. Our calculations show that for the $k_i = 0$ planes the invariant is 1, while for the $k_i = \pi$ planes the invariant is -1 (here $i = x, y, z$). These results indicate the existence of the strong $\mathbb{Z}_2$ Fu-Kane-Mele topological index in the YH_3 material.

As is well known, topological insulators are materials that can provide a platform to reach a large spin Hall conductivity (SHC) signal [7,8]. For the case of YH_3, we have plotted the SHC as a function of Fermi level in Fig. 3(e). In Fig. 3(g) we found a strong SHC response at the Fermi level, well distributed all around the quasinodal sphere. Note that the shape of the signal of the SHC along Γ-M matches that of the model Hamiltonian presented in Fig. 1(a). This particular feature has also been observed in 2D topological insulators, where the **k**-resolved SHC signal is distributed around the Γ point [41]. Furthermore, it is important to highlight that a strong SHC signal is observed in the absence of energy states at the Fermi level, as can be observed in the total density of states calculation in Fig. 3(f). These results indicate that hydride materials can be promissory materials to efficient spin/charge conversion by means of the SHE [42].

B. Calcium telluride

Calcium telluride (CaTe) is another material with quasinodal sphere realization due to band inversion. CaTe is a nonmagnetic material whose space group is Pm-$3m$ no. 221 and it has 48 symmetry operations. This symmetry group can be generated by the operations C_{2z}, C_{2y}, $C_{2(x+y)}$, $C_{3(x+y+z)}$, $\mathcal{I}$, and $\mathbb{T}$. The cubic crystal structure and Brillouin zone for the CaTe compound are shown in Figs. 4(a) and 4(b), respectively. In Fig. 4(d) we present the electronic band structure with the orbital-projected Ca-p states. We note a band character inversion between the valence and conduction bands around the M point. The symbols + and − in Fig. 4(d) indicate a reversal of the inversion symmetry eigenvalues at the M point, which indicates a topological response on this compound.

We have also found a Dirac point (DP) along the M-R **k**-path that can be observed in the band structure of Fig. 4(e). However, a tiny band gap is observed along any **k**-path starting from M when the SOC is taken into account. The stability of the DP is confirmed by the projection of the C_{4x} rotation symmetry eigenvalues at the two bands that generate the DP as shown in Fig. 4(e). The eigenvalues of C_{4x} are the fourth roots of -1, and by Kramer's rule they come in pairs: $(e^{i\frac{\pi}{2}}, e^{-i\frac{\pi}{2}})$ and $(e^{i\frac{3\pi}{2}}, e^{-i\frac{3\pi}{2}})$. The trace of the associated matrix permits us to detect the type of corepresentation at the high-symmetry line, and these traces are $\sqrt{2}$ and $-\sqrt{2}$, respectively. Whenever the traces differ, it means that the bands have different corepresentations of the group generated by C_{4x} and $\mathcal{I}\mathbb{T}$ and therefore the bands cannot hybridize [43]. In this particular case, the traces of the operator C_{4x} are different and therefore the DP is protected by the fourfold rotation symmetry.

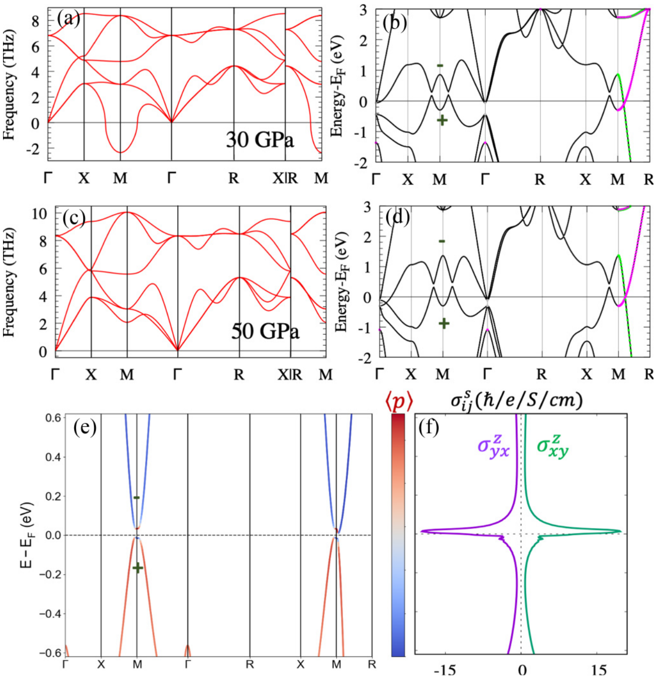

FIG. 5. Top four panels: dynamical stability of cubic CaTe under high pressure. Parts (a) and (c) correspond to phonon dispersion curves at 30 and 50 GPa, respectively. Electronic band structure at the same given pressures is contained in panels (b) and (d) with preserved band inversion at the Γ point. The colors indicate the eigenvalues of the fourfold rotation C_{4x}. Bottom two panels: CaTe with a small ($\epsilon = 3\%$) diagonal distortion, thus breaking the fourfold symmetry. (e) Electronic band structure with gapless phase; note that there is no DP due to the broken fourfold symmetry. (f) Energy-resolved spin Hall conductivity. The SHC arises mainly from the electronic bands that generate the quasinodal sphere, and it survives despite the absence of the DP.

The procedure for finding the quasinodal sphere was also applied in the CaTe case. The quasinodal spheres are centered at the M points, and the signal of the **k**-resolved spin Berry curvature peaks at the **k**-points where the quasinodal sphere is located, as shown in Fig. 4(g). We found that the SHC response of the quasinodal sphere arises from the band inversion around the M point, as illustrated in Fig. 1(b) obtained from the $\mathbf{k} \cdot \mathbf{p}$ Hamiltonian model of Eq. (1). In the case of CaTe, this feature is noticed, namely that the regions near the quasinodal sphere (M-point centered) retain locally large **k**-resolved SHC [see Fig. 4(g)].

Topological insulators share a strong spin Hall conductivity, however the presence of a Dirac point is not always an indication of SHC. We have found a large signal of the SHC at the Fermi level for the CaTe as shown in Fig. 4(f), where the spin Hall conductivity as a function of Fermi energy is presented. We can notice that the SHC signal is strong and coincides with the energy range of the quasinodal sphere and the DP. However, it is not clear whether the signal of the SHC comes from the quasinodal sphere, the DP, or both. To distinguish the contribution to the spin Hall conductivity by the DP and the quasinodal sphere, we have applied a small (3%) diagonal distortion on the cubic CaTe. This strain deformation transforms CaTe from the cubic (Pm-$3m$) to the rhombohedral (R-$3m$) structure. The deformation preserves the symmetry generators: $C_{2(x+y)}$, $C_{3(x+y+z)}$, $\mathcal{I}$, and $\mathbb{T}$, but it breaks the C_{4x} symmetry. The breaking of the C_{4x} symmetry leads to a band gap, and a subsequent absence of the DP is noticed [see Fig. 5(e)].

The rhombohedral structure of CaTe preserves the band inversion, the reversal of the inversion symmetry eigenvalues, and the quasinodal sphere around the M point. For this rhombohedral phase, there is a topological insulator behavior with a small band gap, similar to the $\mathrm{YH_3}$ case and the four-state Hamiltonian model of Eq. (1). The calculation shows a nonzero SHC in the band gap, which emerges from the band inversion at the quasinodal sphere as shown in Fig. 5(f) and corroborated by the $\mathbf{k}\cdot\mathbf{p}$ model [Fig. 1(b)].

The CaTe crystalline phase displayed in Fig. 4(a) has been experimentally known to be dynamically stable for pressures above 33 GPa [44]. This has also been corroborated by our *ab initio* calculations [see Figs. 5(a) and 5(c)]. We can see that the DP along the M-R **k**-path is preserved even when an isotropic pressure is applied [see Figs. 5(b) and 5(d)]. This result is expected since the C_{4x} symmetry, band inversion, and quasinodal sphere are not affected by an isotropic compression.

Our results suggest that CaTe and $\mathrm{YH_3}$ could both display large spin Hall angles for practical applications since they show small longitudinal conductivities (low density of states) at the Fermi level. The SHC signal is concentrated at the hybridized band regions, as was also found by Lau *et al.* [45].

C. Computational methods

For $\mathrm{YH_3}$ and CaTe materials, we have carried out *ab initio* calculations within the density-functional theory with a uniform **k**-mesh in the Brillouin zone of 13 × 13 × 11 and 14 × 14 × 14, respectively. The energy cutoff was taken to be 520 eV and the exchange-correlation contribution to the total energy treated within the PBE parametrization [46], as implemented in the Vienna *ab initio* simulation package (VASP) [47]. Projected band structures were plotted using the PYPROCAR program [48]. The symmetry eigenvalues along the high-symmetry lines were calculated using the IRREP code [49]. To estimate the spin-transport properties, we employed the WANNIER90 code [50,51] to build a Wannier Hamiltonian. The intrinsic spin Hall conductivity (SHC) was evaluated by integrating the spin Berry curvature on a dense 240 × 240 × 240 grid in the first Brillouin zone, using the LINRES code [52]. In this model, the SHC can be written as

$$\sigma^z_{xy} = -\frac{e^2}{\hbar}\sum_n \int_{\mathrm{BZ}} \frac{dk^3}{(2\pi)^3} f_n(k)\Omega^z_{n,xy}(k), \tag{35}$$

where $f_n(k)$ is the Fermi-Dirac distribution and $\Omega^z_{n,xy}(k)$ is the spin Berry curvature for the nth band. The spin Berry curvature for the nth band can be calculated using the Kubo formula:

$$\Omega^z_{n,xy}(k) = -2\hbar^2 \mathrm{Im} \sum_{m\neq n} \frac{\langle n,k|\widehat{j^z_x}|m,k\rangle\langle m,k|\widehat{v}_y|n,k\rangle}{(\epsilon_{n,k}-\epsilon_{m,k})^2}, \tag{36}$$

where $|n,k\rangle$ are the Bloch functions, k is the Bloch wave vector, $\epsilon_{n,k}$ is the electronic band energy, $\hat{v}_i$ is the velocity operator in the i direction, and $\hat{j}^z_x = \frac{1}{2}\{\hat{v}_x, \hat{s}_z\}$ is the spin-current operator.

Vibrational frequencies have been calculated within the perturbation theory method as implemented in VASP using the PHONOPY code [53] to obtain the force constants and vibrational frequencies. In this case, we have used a 2 × 2 × 2 supercell with an 8 × 8 × 8 **q**-mesh to guarantee convergence up to 0.1 cm^{-1}.

IV. CONCLUSIONS

Band inversion in topological insulators induced by hybridization of the energy bands produces quasinodal spheres. The orbital-type change on the bands occurs on the quasinodal sphere, and the matrix information on how this change is happening encodes the strong Fu-Kane-Mele invariant. The signal of the SHC is localized where the orbital type changes, and therefore the signal is strong close to the Fermi level, where hybridization occurs.

The appearance of quasinodal spheres on materials with band inversion due to hybridization is therefore enforced. The change of orbital type must occur in a two-dimensional sphere, otherwise the Fu-Kane-Mele invariant is forced to be trivial.

The band inversion on $\mathrm{YH_3}$ and CaTe is confirmed and the SHC is calculated in both materials. The signal is localized on the quasinodal sphere, and, by removing the Dirac point of CaTe by strain, it is shown that in both cases the signal of the SHC is localized on the quasinodal spheres where the orbital type changes. This result is expected to hold in materials with a similar type of band inversion as the trihydrides ($X\mathrm{H_3}$, $X =$ Y,Gd,Ho,Tb,Nd) and $\mathrm{Si_3N_2}$.

ACKNOWLEDGMENTS

R.G-H. gratefully acknowledges the computing time granted on the supercomputer Mogon at Johannes Gutenberg University Mainz [54]. C.P. thanks the Royal Society of the UK for an International Collaboration Award and the Science and Technology Facilities Council of the UK for computing time on SCARF. B.U. acknowledges the support of CONACYT through Project No. CB-2017-2018-A1-S-30345-F-3125. R.G-H. and B.U. gratefully acknowledge the continuous support of the Alexander Von Humboldt Foundation, Germany.

---

[1] D. Castelvecchi, Nature (London) **547**, 272 (2017).

[2] A. P. Schnyder, S. Ryu, A. Furusaki, and A. W. W. Ludwig, Phys. Rev. B **78**, 195125 (2008).

[3] B. Q. Lv, T. Qian, and H. Ding, Rev. Mod. Phys. **93**, 025002 (2021).

[4] A. Bansil, H. Lin, and T. Das, Rev. Mod. Phys. **88**, 021004 (2016).

[5] C. L. Kane and E. J. Mele, Phys. Rev. Lett. **95**, 226801 (2005).

[6] B. A. Bernevig and S.-C. Zhang, Phys. Rev. Lett. **96**, 106802 (2006).

[7] X.-L. Qi and S.-C. Zhang, Phys. Today **63**, 33 (2010).

[8] J. Sinova, S. O. Valenzuela, J. Wunderlich, C. H. Back, and T. Jungwirth, Rev. Mod. Phys. **87**, 1213 (2015).

[9] L. Fu, C. L. Kane, and E. J. Mele, Phys. Rev. Lett. **98**, 106803 (2007).

[10] A. A. Soluyanov and D. Vanderbilt, Phys. Rev. B **83**, 235401 (2011).

[11] C. L. Kane and E. J. Mele, Phys. Rev. Lett. **95**, 146802 (2005).

[12] Z. Zhu, Y. Cheng, and U. Schwingenschlögl, Phys. Rev. B **85**, 235401 (2012).

[13] Y. Ando, J. Phys. Soc. Jpn. **82**, 102001 (2013).

[14] A. Manchon, H. C. Koo, J. Nitta, S. M. Frolov, and R. A. Duine, Nat. Mater. **14**, 871 (2015).

[15] A. J. Browne, A. Krajewska, and A. S. Gibbs, J. Mater. Chem. C **9**, 11640 (2021).

[16] P. Dziawa, B. J. Kowalski, K. Dybko, R. Buczko, A. Szczerbakow, M. Szot, E. Łusakowska, T. Balasubramanian, B. M. Wojek, M. H. Berntsen *et al.*, Nat. Mater. **11**, 1023 (2012).

[17] Y. Zhang, K. He, C.-Z. Chang, C.-L. Song, L.-L. Wang, X. Chen, J.-F. Jia, Z. Fang, X. Dai, W.-Y. Shan *et al.*, Nat. Phys. **6**, 584 (2010).

[18] W. Witczak-Krempa, G. Chen, Y. B. Kim, and L. Balents, Annu. Rev. Condens. Matter Phys. **5**, 57 (2014).

[19] S. Chege, P. Ning'i, J. Sifuna, and G. O. Amolo, AIP Adv. **10**, 095018 (2020).

[20] H. Zhang, C.-X. Liu, X.-L. Qi, X. Dai, Z. Fang, and S.-C. Zhang, Nat. Phys. **5**, 438 (2009).

[21] M. Zhao, X. Zhang, and L. Li, Sci. Rep. **5**, 16108 (2015).

[22] H. Lin, L. A. Wray, Y. Xia, S. Xu, S. Jia, R. J. Cava, A. Bansil, and M. Z. Hasan, Nat. Mater. **9**, 546 (2010).

[23] S. Chadov, X. Qi, J. Kübler, G. H. Fecher, C. Felser, and S. C. Zhang, Nat. Mater. **9**, 541 (2010).

[24] D. Xiao, Y. Yao, W. Feng, J. Wen, W. Zhu, X.-Q. Chen, G. M. Stocks, and Z. Zhang, Phys. Rev. Lett. **105**, 096404 (2010).

[25] B. A. Bernevig, T. L. Hughes, and S.-C. Zhang, Science **314**, 1757 (2006).

[26] W. Feng, D. Xiao, J. Ding, and Y. Yao, Phys. Rev. Lett. **106**, 016402 (2011).

[27] D. Shao, T. Chen, Q. Gu, Z. Guo, P. Lu, J. Sun, L. Sheng, and D. Xing, Sci. Rep. **8**, 1467 (2018).

[28] J. Wang, Y. Liu, K.-H. Jin, X. Sui, L. Zhang, W. Duan, F. Liu, and B. Huang, Phys. Rev. B **98**, 201112(R) (2018).

[29] R. González-Hernández, E. Tuiran, and B. Uribe, Phys. Rev. B **104**, 205128 (2021).

[30] M. F. Atiyah, *K-theory* (Benjamin, New York, 1967), lecture notes by D. W. Anderson.

[31] G. De Nittis and K. Gomi, Commun. Math. Phys. **339**, 1 (2015).

[32] M. F. Atiyah, Q. J. Math **17**, 367 (1966).

[33] G. Luke and A. S. Mishchenko, *Vector Bundles and Their Applications*, Vol. 447 of *Mathematics and Its Applications* (Kluwer Academic, Dordrecht, 1998).

[34] J. L. Dupont, Math. Scand. **24**, 27 (1969).

[35] J. Ahn and B.-J. Yang, Phys. Rev. B **99**, 235125 (2019).

[36] Z. Wang, X.-L. Qi, and S.-C. Zhang, New J. Phys. **12**, 065007 (2010).

[37] T. L. Hughes, E. Prodan, and B. A. Bernevig, Phys. Rev. B **83**, 245132 (2011).

[38] J. Liu and D. Vanderbilt, Phys. Rev. B **92**, 245138 (2015).

[39] K. Momma and F. Izumi, J. Appl. Crystallogr. **44**, 1272 (2011).

[40] P. Rizo-Acosta, F. Cuevas, and M. Latroche, J. Mater. Chem. A **7**, 23064 (2019).

[41] S.-j. Zhang, W.-x. Ji, C.-w. Zhang, P. Li, and P.-j. Wang, Sci. Rep. **7**, 45923 (2017).

[42] X. Zuo, Q. Gao, X. Sui, X. Xu, X. Jiang, L. Han, H. Li, D. Li, D. Liu, B. Huang *et al.*, Phys. Rev. B **103**, 125159 (2021).

[43] R. González-Hernández, E. Tuiran, and B. Uribe, Phys. Rev. B **103**, 235143 (2021).

[44] H. Luo, R. G. Greene, K. Ghandehari, T. Li, and A. L. Ruoff, Phys. Rev. B **50**, 16232 (1994).

[45] Y.-C. Lau, H. Lee, G. Qu, K. Nakamura, and M. Hayashi, Phys. Rev. B **99**, 064410 (2019).

[46] J. P. Perdew, K. Burke, and M. Ernzerhof, Phys. Rev. Lett. **77**, 3865 (1996).

[47] G. Kresse and J. Furthmüller, Phys. Rev. B **54**, 11169 (1996).

[48] U. Herath, P. Tavadze, X. He, E. Bousquet, S. Singh, F. Muñoz, and A. H. Romero, Comput. Phys. Commun. **251**, 107080 (2020).

[49] M. Iraola, J. L. Mañes, B. Bradlyn, M. K. Horton, T. Neupert, M. G. Vergniory, and S. S. Tsirkin, Comput. Phys. Commun. **272**, 108226 (2022).

[50] A. A. Mostofi, J. R. Yates, G. Pizzi, Y.-S. Lee, I. Souza, D. Vanderbilt, and N. Marzari, Comput. Phys. Commun. **185**, 2309 (2014).

[51] G. Pizzi, V. Vitale, R. Arita, S. Blügel, F. Freimuth, G. Géranton, M. Gibertini, D. Gresch, C. Johnson, T. Koretsune *et al.*, J. Phys.: Condens. Matter **32**, 165902 (2020).

[52] J. Železný, https://bitbucket.org/zeleznyj/wannier-linear-response/wiki/Home.

[53] A. Togo and I. Tanaka, Scr. Mater. **108**, 1 (2015).

[54] hpc.uni-mainz.de.